1985

Homogeneous nucleation rate measurements. I. Ethanol, n-propanol, and i-propanol

Atul Kacker

Richard H. Heist
Fairfield University, rheist@fairfield.edu

Published Citation

Kacker, A., & Heist, R. H. (1985). Homogeneous nucleation rate measurements. I. Ethanol, n-propanol, and i-propanol. The Journal of chemical physics, 82(6), 2734-2744. https://doi.org/10.1063/1.448271.

Homogeneous nucleation rate measurements. I. Ethanol, *n*-propanol, and *i*-propanol

Atul Kacker and Richard H. Heist[a)]
Department of Chemical Engineering, University of Rochester, Rochester, New York 14627

(Received 9 November 1984; accepted 29 November 1984)

Homogeneous nucleation rate measurements have been made on ethanol, *n*-propanol, and *i*-propanol vapors over a range of temperatures and supersaturations. The Becker–Doring–Zeldovitch nucleation rate expression has been scaled so as to give good agreement with the measured nucleation rates. The same scaling factors are also used to compare calculated critical supersaturations with experimental data obtained from this investigation and a variety of other sources. The agreement is good in all cases. The nucleation rate measurements and the critical supersaturation data from this investigation reveal anomalous behavior for ethanol near 260 K and for *n*-propanol near 275 K.

INTRODUCTION

For nearly a century much effort has been devoted to attempts to quantify the basic physics of the nucleation process. The literature is replete with theoretical and experimental work designed to extend the current level of understanding or to confirm or disprove existing models. One feature common to most of the experimental investigations is the measurement of the supersaturation giving rise to the onset of nucleation (typically, a nucleation rate of one event—drop, bubble, crystal, etc.—per cubic centimeter per second) either at one temperature or over a range of temperatures. This is usually referred to as the critical supersaturation. In many instances, researchers have found what appears to be rather good agreement between the measured critical supersaturation and that predicted using nucleation theory. As an example, consider the critical supersaturation measurements which have been published for water vapor.[1] Over the entire range of temperature (about 35 deg), the measured and predicted critical supersaturations differ by less than 10%. At first glance this seems reasonably impressive; but if one compares the measured and the predicted nucleation rates, "agreement" is now within several orders of magnitude rather than 10%. Clearly, the critical supersaturation measurements by themselves can be misleading. They are not adequate to serve as a quantitative test of a nucleation theory because they lack the necessary sensitivity for detailed comparison of theory and experiment. It is essential that nucleation rate studies be done to provide a satisfactory test of a nucleation theory.

Fortunately, progress has been made in this direction. Much of the published research involves transient measurements carried out using carefully controlled expansion cloud chambers.[2–5] Most of the early problems involving reproducible expansion paths, accurate droplet counting, and uniform sensitive times have been largely solved; and nucleation rate data over relatively large ranges is becoming available. An important advantage of the expansion cloud chamber is that large nucleation rates (up to about 10^9) can be measured.[6] Two limitations are the short sensitive times (1–10 ms) and the difficulty in measuring smaller nucleation rates (less than several hundred drops/cm^3/s).

The thermal diffusion cloud chamber (TDCC) is only now beginning to be used for nucleation rate measurements.[7–11] The TDCC eliminates several of the disadvantages associated with the expansion cloud chamber, but, in turn, contributes a few of its own. The significant advantages of the TDCC are the overall simplicity of operation and construction, the steady state mode of operation, the self-cleaning nature of the chamber and the possibility of making continuous nucleation rate measurements. Two significant disadvantages are the need for a comprehensive set of thermodynamic and hydrodynamic data to determine the pressure and temperature conditions inside the chamber and the need to operate above the triple point of the working fluid.[12] The most serious limitation, however, has been that only data obtained from small nucleation rate measurements (less than about 5 drops/cm^3/s) could be used with any confidence because of the deleterious effect the nucleated droplets had on the vapor concentration and temperature inside the chamber.

Recently, the role of nucleation and growth in the TDCC has been investigated, and a model which successfully accounts for the effects of vapor depletion and latent heat generation has been published.[10,11] Using this model and an electronic counting system, it is possible to make nucleation rate measurements in a TDCC ranging as low as 10^{-2} and up to about 10^3 drops/cm^3/s. This capability is important since it not only extends the range of available nucleation rate data, but it also allows for direct comparison of expansion cloud chamber and diffusion cloud chamber rate data because of the overlap in the ranges of the two methods.

a) Author to whom all correspondence should be addressed.

 0021-9606/85/062734-11$02.10

In this paper we present results of homogeneous nucleation rate measurements obtained at a variety of temperatures for ethanol, *n*-propanol, and *i*-propanol. First, TDCC operation, the electronic counting system, and the method used to measure the droplet radii are described briefly. Next, the model for the role of vapor depletion and latent heat is reviewed. Finally, the nucleation rate data are presented and discussed.

THERMAL DIFFUSION CLOUD CHAMBER

The general description of the TDCC and its operation is available elsewhere.[13–18] We provide a schematic in Fig. 1 and comment only on those points which are peculiar to the chamber used in this research. The TDCC used for these measurements consisted of two aluminum plates of cylindrical geometry, 0.203 m in diameter and 0.02 m thick. The plates were separated by a Pyrex ring 0.0254 m high. The temperature of each plate was controlled to within 0.1 K by constant temperature circulator baths attached to each plate. The surface temperature of the working fluid pool was measured with a chromel–constantan thermocouple inserted through the bottom plate, with the junction barely dimpling the surface of the pool. The top plate thermocouple was mounted in the plate just above the surface interior to the chamber. During the rate measurements a dc electric field (150 V/cm) was maintained across the plates to remove charged particles.

During a nucleation rate experiment, a steady flux of droplets is observed which originate in a narrow zone located in the upper part of the chamber. At low rates, the thickness (vertical dimension) of the nucleation zone can be measured directly with a cathetometer. As the temperature difference between the plates is increased one observes a rapid increase in droplet flux, an increase in the size of the droplets and an increase in the nucleation zone thickness. At higher droplet fluxes, the lower boundary of the nucleation zone is obscured by the falling droplets, and the zone thickness can no longer be measured visually. It should be mentioned that, even though we refer to "higher droplet fluxes," experimental conditions are such that we are well below the oscillatory nucleation regime described in Refs. 7 and 10.

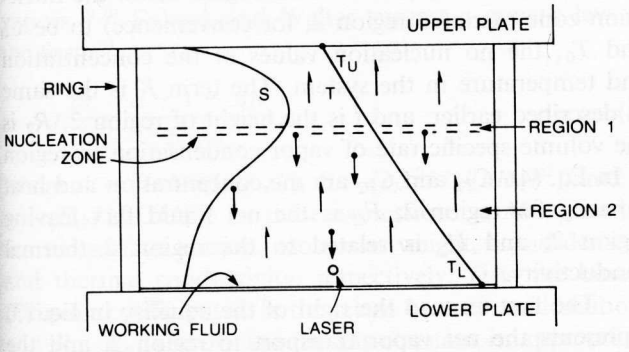

FIG. 1. Diffusion cloud chamber schematic (not to scale) illustrating regions 1 and 2 used in the vapor depletion and latent heat model described in the text. Representative temperature and supersaturation profiles and a nucleation zone are shown. The vapor flux, the droplet flux, and the counting system laser are indicated.

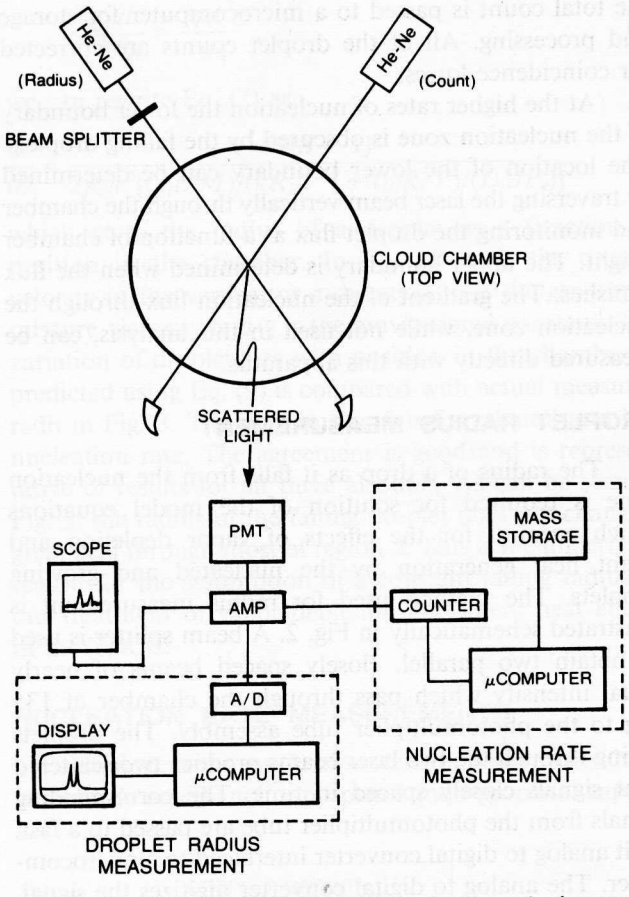

FIG. 2. Schematic of the experimental setup for the nucleation rate and droplet radius measurements described in the text.

NUCLEATION FLUX MEASUREMENT

As is shown in Fig. 1, the nucleated drops fall from the nucleation zone, through the chamber to the lower plate pool of working fluid. A portion of this droplet flux passes through a helium–neon laser beam passing through the chamber near the lower plate pool. The laser beam is focused into the center of the chamber using a long focal length double convex lens. The beam can be translated vertically throughout the chamber so that droplet fluxes can be measured at any point below or in the nucleation zone. The light scattered as a droplet falls through the laser is detected by a photomultiplier assembly, and after some conditioning the resulting signal is passed to a droplet counter. This is illustrated schematically in Fig. 2.

The droplet counter has a threshold setting which enables us to eliminate small signals arising from droplets passing through low intensity regions of the laser beam (e.g., edges, reflected beams). From the known laser beam geometry and a direct measurement of the portion of the laser beam visible to the photomultiplier tube the counting area in the chamber can be determined. Since the droplet flux is related to the droplet count through the counting area, it is essential that the counting area be known.

When the signal to the counter satisfies the discriminator criteria, a count is recorded. The counts are accumulated over a set period of time, determined by a selectable time base, and at the end of that period of time

the total count is passed to a microcomputer for storage and processing. All of the droplet counts are corrected for coincidence losses.

At the higher rates of nucleation the lower boundary of the nucleation zone is obscured by the falling droplets. The location of the lower boundary can be determined by traversing the laser beam vertically through the chamber and monitoring the droplet flux as a function of chamber height. The upper boundary is determined when the flux vanishes. The gradient of the nucleation flux through the nucleation zone, while not used in this analysis, can be measured directly with this apparatus.

DROPLET RADIUS MEASUREMENT

The radius of a drop as it falls from the nucleation zone is required for solution of the model equations which account for the effects of vapor depletion and latent heat generation by the nucleated and growing droplets. The method used for radius measurement is illustrated schematically in Fig. 2. A beam splitter is used to obtain two parallel, closely spaced beams of nearly equal intensity which pass through the chamber at 135 deg to the photomultiplier tube assembly. The droplets falling through the two laser beams produce two scattered light signals closely spaced in time. The corresponding signals from the photomultiplier tube are passed to a fast, 8 bit analog to digital converter interfaced to a microcomputer. The analog to digital converter digitizes the signal, and the information is stored in the computer. With this information and the known sampling rate, the time between the two signal peaks can be determined. This information, together with the known separation of the two laser beams, gives the droplet velocity. Stokes' law is assumed to apply, and the falling radius can then be obtained from the droplet velocity. The beam splitter can be translated vertically thus allowing the droplet size to be measured at any height in the chamber.

VAPOR DEPLETION AND LATENT HEAT EFFECTS

As illustrated in Fig. 1, the portion of the TDCC containing droplets can be conveniently divided into two regions: region 1 the nucleation zone; and region 2 the portion of the chamber below the nucleation zone. Droplets are nucleated and grow to macroscopic size in the nucleation zone and then pass out of the nucleation zone and fall through region 2 to the liquid pool on the lower plate. As the droplets grow in both regions, the condensable vapor is depleted and the temperature profile in the TDCC is disturbed. Since we need to know the supersaturation and temperature in the nucleation zone, it is necessary to account for both these effects.

Subject to certain assumptions described in detail elsewhere,[9,10] the following mass and energy conservation equations for the nucleation zone in the TDCC and the region below the nucleation zone can be written down. First, for the nucleation zone,

$$dC_1/dt = K[C_2 - C_1]/\delta - R_1 \quad (1)$$

and

$$C_{T1}C_{P1}dT_1/dt = K[C_2 - C_1][\Delta H_V(T_1)]/\delta - F_{l1}[\Delta H_l(T_1)] - U_1[T_1 - T_0] + U_1'[T_2 - T_1]. \quad (2)$$

Next for region 2, below the zone,

$$dC_2/dt = K[C_0 - C_2]/l - R_2 \quad (3)$$

and

$$C_{T2}C_{P2}dT_2/dt = K[C_0 - C_2][\Delta H_V(T_2)]/l - F_{l2}[\Delta H_l(T_2)] - U_2[T_2 - T_1]. \quad (4)$$

In Eq. (1) C_2 is the concentration of the diffusing vapor entering the nucleation zone, C_1 is the zone vapor concentration, K is a proportionality term which is, in general, concentration and temperature dependent and must be determined for each experiment and δ is the zone height, and R_1 is the "reaction" term which expresses the volume specific rate of conversion of working fluid vapor to liquid by nucleation and growth. In general, R_1 is a complicated function of concentration and temperature and requires both a reliable nucleation rate expression and an appropriate droplet growth law or knowledge of the droplet size distribution in the nucleation zone as a function of time. The R_1 term is discussed in more detail in Ref. 10.

In Eq. (2) T_2 and T_1 are the input and the zone temperatures, respectively; C_{T1} is the total concentration (vapor plus carrier gas) in the zone; C_{P1} is the zone heat capacity; $\Delta H_V(T_1)$ and $\Delta H_l(T_2)$ are the vapor and liquid enthalpies, respectively, for the working fluid; F_{l1} is the liquid flux leaving the zone; T_0 is the zone temperature computed assuming no nucleation; and U_1 and U_1' are related to the zone thermal conductivity. The first term on the right of the equality in Eq. (2) represents the net enthalpy transport into the zone due to vapor transport. The temperature dependence of the vapor enthalpy has been suppressed. The second term is net enthalpy transport out of the zone due to liquid transport; and, again, the temperature dependence of the enthalpy has been suppressed. The last two terms in Eq. (2) represent net energy transport from the zone by conduction.

In Eqs. (3) and (4), we have chosen the concentration and temperature "profiles" in the region below the nucleation zone (denoted region 2, for convenience) to be C_0 and T_0, the no nucleation values of the concentration and temperature in the system. The term K is the same as described earlier, and l is the height of region 2. R_2 is the volume specific rate of vapor condensation in region 2. In Eq. (4), C_{T2} and C_{P2} are the concentration and heat capacity for region 2; F_{l2} is the net liquid flux leaving region 2; and U_2 is related to the region 2 thermal conductivity.

The first term to the right of the equality in Eq. (3) represents the net vapor transport to region 2, and the second term represents the vapor transport to the droplets as they pass through region 2. Similarly, in Eq. (4), the first term is the net enthalpy transport to region 2, the second term represents the net enthalpy transport to the

droplets as they pass through region 2 falling to the lower plate, and the last term represents net energy transport from region 2 by conduction.

At steady state the right hand sides of Eqs. (1)–(4) vanish giving rise to four algebraic equations relating the concentration and temperature in and below the nucleation zone. Under these conditions, the reaction term R_1 in Eq. (1) becomes[11]

$$R_1 = \rho_l v_m [n_f J]. \tag{5}$$

In Eq. (5), J is the steady state nucleation rate, ρ_l is the liquid density, v_m is the molecular volume of the condensing vapor, and n_f is the number of molecules in a droplet in excess of the critical size as it falls from the nucleation zone.

At steady state, F_{l1} in Eq. (2) becomes identical to R_1 in Eq. (5), and R_2 and F_{l2} in Eqs. (3) and (4) assume the following form[11]:

$$R_2 = F_{l2} = \frac{4_\pi r_f D_{12} J \delta t_f}{l} [C_2 - C_{2e}(T_2)]. \tag{6}$$

Where t_f is the passage time of the droplet through region 2, r_f is the radius of the droplet as it falls from the nucleation zone, D_{12} is the binary diffusion coefficient and $C_{2e}(T_2)$ is the equilibrium vapor concentration at T_2. The other symbols have been defined previously. In deriving Eq. (6) we made use of a conventional droplet growth law expression,[19] and we assumed that the size of the droplet does not change as it falls through region 2. This last assumption will be discussed later. Substituting Eqs. (5) and (6) into the steady state version of Eqs. (1)–(4) along with experimental values for J, r_f, lower $T(L)$ and upper $T(U)$ plate temperatures, and total pressure P_T gives, upon solution, the zone supersaturation and temperature corrected for the effects of vapor depletion and latent heat in the TDCC.[11]

DROPLET GROWTH

Although we are able to measure the droplet radii at discrete points in the chamber, it is necessary to know the radius as a continuous function of the chamber height in order to solve Eqs. (1)–(4) above. There are a number of growth laws available in the literature which can predict the size change of droplets in supersaturated vapors.[19,20] Fukuta and Walter suggest a growth law of the form[20]

$$r\frac{dr}{dt} = \frac{S - 1 - A/r}{B + C}, \tag{7}$$

where $A = (2\sigma M)/(\rho_l R_A T)$, $B = (\rho_l L^2 M)/(k R_B T^2)$, and $C = (\rho_l R_C T)/(DMP_e)$. In these expressions σ, M, ρ_l, and k are the surface tension, molecular weight, liquid density, and thermal conductivity, respectively. D is the binary diffusion coefficient, L is the latent heat of condensation, and R_A, R_B, and R_C are the gas constant in appropriate units. In Eq. (7) S is the vapor supersaturation and r is the droplet radius. Under the conditions of our experiments we shall ignore the Kelvin term; and, using Stokes' law,

$$v_z = \frac{dz}{dt} = \frac{2\rho_l r^2 g}{9\eta}, \tag{8}$$

we can rewrite Eq. (7) as

$$\frac{dr}{dz} = \frac{9\eta(S-1)}{2\rho_l g r^3 [(\rho_l L^2 M)/(kR_B T^2) + (\rho_l R_C T)/(DMP_e)]}, \tag{9}$$

which gives the radius of a droplet as a function of position in the chamber. In Eq. (8) v_z is the droplet velocity in the vertical or z direction, η is the gas–vapor mixture viscosity and g is the gravitational constant. The variation of droplet size with position in the chamber as predicted using Eq. (9) is compared with actual measured radii in Fig. 3. The data in Fig. 3 is for ethanol at a low nucleation rate. The agreement is good and is representative of results for all three alcohols. As can be seen in Fig. 3, the radius of the falling droplet does not change a great deal through most of region 2. This is the underlying reason for the assumption of a constant falling radius in our treatment of vapor depletion and latent heat effects in the TDCC.

NUCLEATION RATE MEASUREMENTS

Homogeneous nucleation rate measurements have been made on ethanol, *n*-propanol and *i*-propanol vapors.

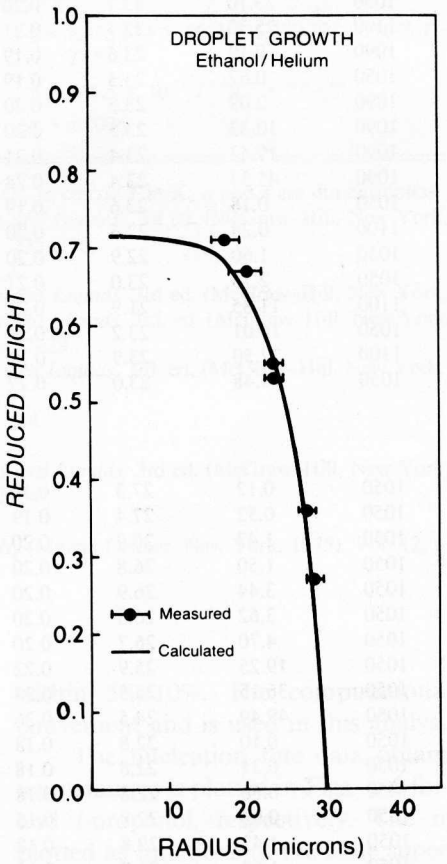

FIG. 3. The variation of droplet size in the TDCC. The points are the measured radii, and the solid curve is calculated using Eq. (9) in the text. The bars through each data point represent the range (one standard deviation) of the droplet radii measured at that reduced chamber height. The lower boundary of the nucleation zone for the experiment illustrated in this figure is approximately at a reduced height of 0.65, and the nucleation zone thickness δ is 0.09 in reduced units.

The experimental data are listed in Table I. In Table I the experiment number is listed first for each alcohol followed by the lower and upper plate temperatures and the total pressure. Next, the measured nucleation flux, the falling radius, and the nucleation zone thickness are listed in the remaining three columns. The thermodynamic and hydrodynamic data used in the analysis is tabulated in Table II.

Since the measured droplet flux data is statistical in nature, the values listed in Table I represent the mean of many individual measurements (corrected for coincidence losses). The statistics of the flux measurements were observed to be Poisson distributed. In fact, the statistical distribution serves as a useful criteria in determining the reliability of a set of experimental data. We have observed, for instance, that the distribution of flux data obtained at low nucleation rates in the absence of an electric field is significantly less Poisson in character.[8]

The nucleation rate is related to the nucleation flux by the nucleation zone thickness. The zone thickness δ listed in Table I, is determined in the following way. Using the BDZ (Becker–Doring–Zeldovitch) nucleation rate expression and the no-nucleation supersaturation and temperature profiles in the TDCC, a nucleation rate

TABLE I. Experimental data obtained from the nucleation rate measurements of ethanol, *n*-propanol, and *i*-propanol vapors. The first column is the experiment number; the next three are the lower plate temperature T_L, the upper plate temperature T_U, and the total pressure P_T, respectively; the fifth column is the measured nucleation flux I; and the next two columns are the falling radius r_f and the nucleation zone thickness δ, respectively.

Run No.	T_L (K)	T_U (K)	P_T (mm Hg)	I (cm^{-2} s^{-1})	r_f (10^{-4} cm)	δ (cm)
Ethanol						
1	291.3	250.2	1050	0.18	24.0	0.18
2	291.3	250.3	1090	0.27	24.0	0.18
3	291.3	249.3	1050	1.90	23.8	0.19
4	291.4	249.3	1050	2.40	23.8	0.19
5	291.2	248.7	1100	8.37	23.9	0.19
6	291.8	248.9	1090	9.95	23.8	0.19
7	292.1	248.9	1090	12.68	23.8	0.19
8	292.8	248.5	1050	23.10	23.7	0.20
9	293.1	247.9	1100	25.30	23.7	0.21
10	301.3	259.4	1090	0.19	23.6	0.19
11	301.5	259.2	1050	0.62	23.5	0.19
12	301.7	258.7	1090	2.09	23.5	0.20
13	302.7	259.0	1090	10.33	23.5	0.20
14	303.2	258.0	1090	19.43	23.4	0.21
15	305.0	256.6	1090	45.57	23.4	0.24
16	320.8	279.8	1050	0.18	23.6	0.19
17	320.6	278.4	1100	0.28	22.3	0.20
18	320.8	278.3	1050	1.60	22.9	0.20
19	321.2	278.2	1050	2.75	23.0	0.21
20	322.1	277.8	1100	11.85	21.9	0.22
21	322.7	278.2	1050	16.01	23.2	0.24
22	321.8	277.0	1100	32.50	23.9	0.22
23	325.1	274.7	1050	74.48	23.0	0.27
n-propanol						
1	331.7	284.3	1050	0.12	27.3	0.19
2	331.3	284.1	1050	0.52	27.4	0.19
3	332.8	284.4	1050	1.47	26.9	0.20
4	332.7	283.9	1050	1.50	26.8	0.20
5	332.1	283.4	1050	3.44	26.9	0.20
6	332.1	283.0	1050	3.62	26.8	0.20
7	332.0	282.8	1050	4.70	26.7	0.20
8	334.4	282.6	1050	19.25	25.9	0.22
9	336.1	280.7	1050	36.15	25.5	0.24
10	337.8	280.3	1050	49.49	24.5	0.26
11	309.7	263.7	1050	0.10	22.8	0.18
12	309.8	263.6	1050	0.21	22.8	0.18
13	309.8	263.6	1050	0.66	22.8	0.18
14	309.9	263.4	1050	0.99	22.8	0.18
15	309.8	263.1	1050	1.42	22.8	0.18
16	310.1	263.5	1050	1.68	22.8	0.18
17	310.7	263.8	1050	2.37	22.9	0.18
18	310.6	263.7	1050	2.99	22.8	0.18
19	310.9	263.5	1050	4.58	22.7	0.18
20	310.7	263.1	1050	4.94	22.7	0.19
21	311.3	262.6	1050	10.90	22.3	0.19
22	294.9	248.3	1050	0.11	16.8	0.20
n-propanol (*continued*)						
23	295.0	248.2	1050	0.44	16.7	0.19
24	295.7	248.7	1050	0.85	16.6	0.21
25	295.6	248.3	1050	1.45	16.6	0.20
26	296.4	247.5	1050	5.54	16.3	0.22
27	297.8	248.2	1050	12.41	16.0	0.23
28	297.8	248.2	1050	12.96	15.2	0.23
i-propanol						
1	325.7	280.7	1200	0.04	23.5	0.19
2	325.8	280.8	1200	0.08	23.5	0.19
3	325.7	280.6	1200	0.35	23.4	0.19
4	325.8	280.5	1200	1.29	23.4	0.20
5	327.1	280.6	1130	3.40	23.3	0.20
6	327.0	280.8	1190	3.61	23.3	0.20
7	327.2	280.5	1200	4.27	23.3	0.21
8	327.3	279.2	1190	13.01	23.1	0.21
9	327.7	279.9	1170	14.14	23.1	0.21
10	327.8	278.7	1150	23.38	23.0	0.21
11	307.6	262.9	1170	0.04	19.2	0.19
12	307.6	262.9	1120	0.16	19.1	0.19
13	308.4	263.3	1170	0.51	19.0	0.19
14	309.2	263.7	1150	0.56	18.6	0.20
15	308.6	263.1	1160	0.60	19.1	0.20
16	308.7	263.2	1160	0.70	19.0	0.20
17	308.3	263.4	1150	0.75	18.3	0.19
18	309.1	263.8	1160	0.87	19.0	0.20
19	309.2	263.5	1160	0.98	18.5	0.20
20	308.6	263.3	1170	1.53	18.5	0.19
21	309.2	263.3	1150	3.37	18.4	0.20
22	309.0	263.4	1120	3.73	18.5	0.20
23	310.0	263.5	1070	5.78	18.4	0.21
24	310.0	263.4	1120	6.47	18.4	0.20
25	309.8	263.0	1120	7.92	18.3	0.21
26	310.9	262.6	1150	15.44	18.3	0.22
27	311.3	260.5	1150	29.54	18.3	0.23
28	311.1	261.9	1190	29.51	18.4	0.22
29	292.6	248.9	1200	0.04	16.4	0.18
30	292.7	249.0	1200	0.18	16.4	0.18
31	292.7	249.0	1200	0.52	16.4	0.18
32	293.0	249.4	1160	1.05	16.3	0.18
33	293.0	249.0	1190	1.95	16.3	0.19
34	292.8	248.3	1190	3.80	16.1	0.19
35	292.8	248.7	1190	3.97	16.2	0.19
36	292.2	247.9	1200	4.13	16.0	0.19
37	292.8	248.2	1150	5.52	15.9	0.19
38	293.2	247.9	1200	10.50	15.8	0.20
39	293.0	247.5	1200	12.14	15.7	0.20
40	294.4	246.9	1200	24.85	15.5	0.21

TABLE II. Thermodynamic and hydrodynamic data for ethanol, *n*-propanol, *i*-propanol, and helium. Expressions are given for the vapor thermal conductivity λ; saturation vapor pressure P_e; surface tension σ; liquid and vapor viscosity η_l and η_v; density ρ_l; molar heat capacity for liquid and vapor C_{pl} and C_{pv}; and values are given for molecular weight M; binary diffusion coefficient D_{ab}; and the binary diffusion coefficient temperature dependence s.[a]

Ethanol

$\lambda = 82.03 \times 10^{-6}[\exp(8.99 \times 10^{-5}\, T) - \exp(-4.6726 \times 10^{-4}\, T)] + 2.68 \times 10^{-10}\, T^2$ [b]

$P = 10 \uparrow (9.336 - 2257/T)$ [c]

$\sigma = 23.88 - 0.008\,07 \times (T - 273.16)$ [p]

$\eta_v = 9.986 \times 10^{-6}\, T^{1.5}/(T + 295.59)$ [e]

$\eta_l = 1.0 \times 10^{-2}\{10 \uparrow [686.64(1/T - 1/300.88)]\}$ [f]

$\rho_l = 1.058 - 1.003 \times 10^{-3}\, T + 2.9 \times 10^{-7}\, T^2$ [g]

$C_{pv} = 2.153 + 5.113 \times 10^{-2}\, T - 2.004 \times 10^{-5}\, T^2 + 3.28 \times 10^{-10}\, T^3$ [h]

$C_{pl} = 24.15 + 0.116(T - 273.15) - 2.0 \times 10^{-4}(T - 273.15)^2$ [i,h]

$M = 46.069$

$\alpha = 0.3$ [j]

D_{ab} (423 K, 1 atm) = 0.821 [k,l]

$s = 0.795$ [k,n]

n-propanol

$\lambda = 6.198\,13 \times 10^{-5}[\exp(8.645\,42 \times 10^{-5}\, T) - \exp(-4.494\,13 \times 10^{-4}\, T)] + 2.460\,71 \times 10^{-10}\, T^2$ [b]

$P_e = \exp(84.695\,722 - 8559.6064/T - 9.29 \log T)$ [o]

$\sigma = 25.28 - 0.083\,94 \times (T - 273.16)$ [p]

$\eta_v = 1.183 \times 10^{-5}\, T^{1.5}/(T + 506.75)$ [m]

$\eta_l = 1.0 \times 10^{-2}\{10 \uparrow [951.04(1/T - 1/327.83)]\}$ [f]

$\rho_l = 0.8201 - 0.8183 \times 10^{-3}(T - 273.15) + 1.08 \times 10^{-6}(T - 273.15)^2 + 16.5 \times 10^{-9}(T - 273.15)^3$ [g]

$C_{pv} = 0.59 + 7.942 \times 10^{-2}\, T - 4.431 \times 10^{-5}\, T^2 + 1.026 \times 10^{-8}\, T^3$ [h]

$C_{pl} = 30.75 + 0.144(T - 273.15) - 2.0 \times 10^{-4}(T - 273.15)^2$ [i,h]

n-propanol (*continued*)

$M = 60.096$

$\alpha = 0.3$ [j]

D_{ab} (423.2 K, 1 atm) = 0.676 [k]

$s = 0.795$ [k,n]

i-propanol

$\lambda = 5.925\,04 \times 10^{-5}[\exp(9.128\,46 \times 10^{-5}\, T) - \exp(-4.745\,22 \times 10^{-4}\, T)] + 2.6248 \times 10^{-10}\, T^2$ [b]

$P_e = \exp[18.6929 - 3640.2/(T - 53.54)]$ [c]

$\sigma = 44.451\,535 - 0.0789T$ [d]

$\eta_v = 0.9183 \times 10^{-5}\, T^{1.5}/(T + 303.49)$ [e]

$\eta_l = 1.0 \times 10^{-2}\{10 \uparrow [1139.7(1/T - 1/323.44)]\}$ [f]

$\rho_l = 0.8014 - 0.809 \times 10^{-3}(T - 273.15) - 2.7 \times 10^{-6}(T - 273.15)^2$ [g]

$C_{pv} = 7.745 + 4.502 \times 10^{-2}\, T + 1.53 \times 10^{-5}\, T^2 - 2.212 \times 10^{-8}\, T^3$ [h]

$C_{pl} = -29.186 + 0.2874T - 1.9 \times 10^{-4}\, T^2$ [h]

$M = 60.096$

$\alpha = 0.3$ [j]

D_{ab} (423 K, 1 atm) = 0.677 [k]

$s = 0.795$ [k,n]

Helium

$\lambda = 7.376\,974 \times 10^{-5} + 1.139\,222 \times 10^{-6}\, T - 6.343\,536 \times 10^{-10}\, T^2$ [m]

$\eta = 145.5 \times 10^{-7}\, T^{1.5}/(T + 74.1)$ [m]

M = 4.0026

[a] λ in cal/(cm s K); P_e in mm Hg; σ in dyn/cm; η in P; C_p in cal/(mol K); D_{ab} in cm^2/s; T in K; α and s are dimensionless.

[b] R. C. Reid, J. M. Prausnitz, and T. K. Sherwood, *The Properties of Gases and Liquids,* 3rd ed. (McGraw-Hill, New York, 1977), pp. 481–494.

[c] *International Critical Tables* (McGraw-Hill, New York, 1929), Vol. 3, pp. 215–218.

[d] J. Phys. Chem. Ref. Data, **1,** 1972.

[e] R. C. Reid, J. M. Prausnitz, and T. K. Sherwood, *The Properties of Gases and Liquids,* 3rd ed. (McGraw-Hill, New York, 1977), pp. 395–409.

[f] R. C. Reid, J. M. Prausnitz, and T. K. Sherwood, *The Properties of Gases and Liquids,* 3rd. ed. (McGraw-Hill, New York, 1977), pp. 634–640.

[g] *International Critical Tables* (McGraw-Hill, New York, 1929), Vol. 3, pp. 27–29.

[h] R. C. Reid, J. M. Prausnitz, and T. K. Sherwood, *The Properties of Gases and Liquids,* 3rd. ed. (McGraw-Hill, New York, 1977), pp. 152–156 and 633–640.

[i] *International Critical Tables,* (McGraw-Hill, New York, 1929), Vol. 3, p. 114.

[j] J. L. Katz and B. J. Ostermier, J. Chem. Phys. **47,** 478 (1962).

[k] R. C. Reid, J. M. Prausnitz, and T. K. Sherwood, *The Properties of Gases and Liquids,* 3rd ed. (McGraw-Hill, New York, 1977), pp. 554–558.

[l] E. N. Fuller, P. D. Shettler, and J. C. Giddings, Ind. Eng. Chem. **58,** 19 (1966).

[m] R. H. Heist and H. Reiss, J. Chem. Phys. **59,** 15 (1973).

[n] J. C. Giddings, E. Grushka, and R. A. Keller, *Advances in Chromatography* (Marcel Dekker, New York, 1975), Vol. 12, p. 128.

[o] T. Schmeling and R. Strey, Ber. Bunsenges. Phys. Chem. **87,** 871 (1983).

[p] R. Strey and T. Schmeling, Ber. Bunsenges. Phys. Chem. **87,** 324 (1983).

profile is calculated for the entire chamber. Because of the strong dependence of nucleation rate on supersaturation and temperature, a sharp peak in the rate profile is obtained in the upper region of the chamber corresponding to the region of maximum nucleation. The convention used in determining the nucleation zone thickness is to set δ equal to the full width of this peak at half the maximum height.[9,10] We have measured the zone thickness using the traversing laser beam assembly described in the nucleation flux measurement section and have found that the measured thickness and the thickness calculated using the above convention generally agree to within 5%–10%. The computational method is more convenient and is used in this analysis.

The nucleation rate data obtained at various zone temperatures is plotted in Figs. 4–6 for ethanol, *n*-propanol and *i*-propanol, respectively. The nucleation rates are plotted as functions of the zone supersaturation obtained from the solution of Eqs. (1)–(4). The solid circles in Figs. 4–6 represent the measured nucleation rate data. The open circles in Fig. 4 represent data obtained for ethanol at 262 K which is typical of the behavior observed for all three alcohols when the nucleation rate is plotted against the zone supersaturation obtained by ignoring the

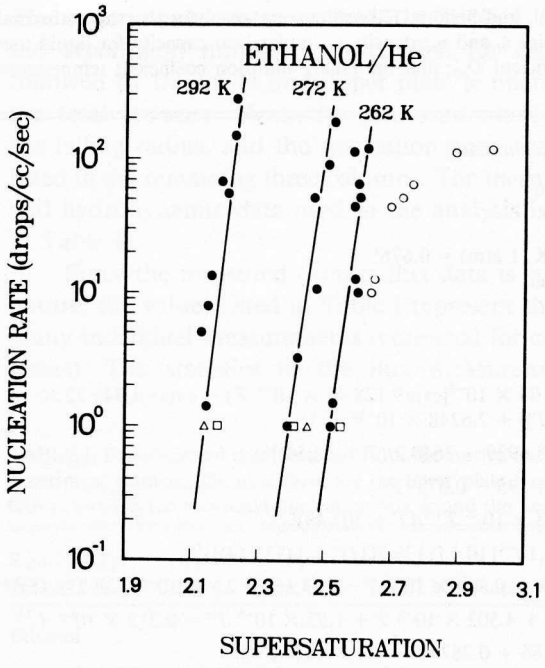

FIG. 4. Variation of homogeneous nucleation rate of ethanol with supersaturation and temperature. The solid circles in each plot are nucleation rate data corrected for vapor depletion and latent heat effects. The open circles, shown only for the lowest temperature data set, correspond to rate data uncorrected for vapor depletion and latent heat effects. The open squares and triangles represent critical supersaturation data obtained from literature sources.[21] The solid lines in each plot were obtained using Eq. (12) in the text and the appropriate values for a and b from Table III.

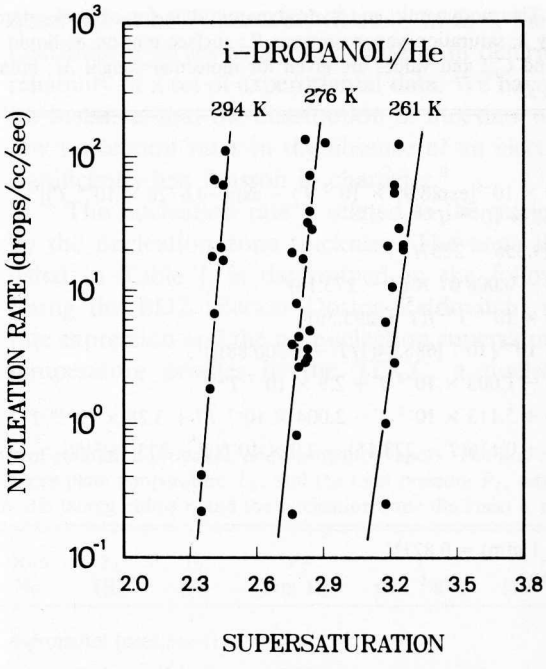

FIG. 6. Variation of homogeneous nucleation rate of *i*-propanol with supersaturation and temperature. The solid circles are the nucleation rate data corrected for vapor depletion and latent heat effects. The solid lines were obtained using Eq. (12) in the text and the appropriate values for a and b from Table III.

presence of the nucleated droplets. For nucleation rates of about 5 drops/cm^3/s and less, the zone supersaturation obtained by ignoring the presence of the nucleated droplets agrees with the zone supersaturation predicted by the solution to Eqs. (1)–(4). As the nucleation rate increases, the difference between the two increases rapidly. Thus, the effect of ignoring nucleation and growth throughout the TDCC, is a significant overestimation of the vapor concentration in the nucleation zone and an underestimation of the zone temperature.

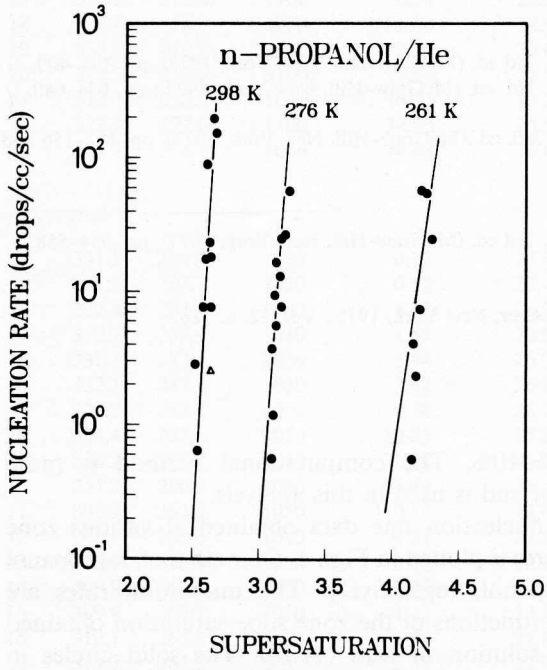

FIG. 5. Variation of homogeneous nucleation rate of *n*-propanol with supersaturation and temperature. The solid circles are the nucleation rate data corrected for vapor depletion and latent heat effects. The open triangle represents literature data for a critical supersaturation measurement.[21] The solid lines were obtained using Eq. (12) in the text and the appropriate values for a and b from Table III.

In Figs. 4 and 5, the open squares and triangles represent critical supersaturation data from the literature.[21] In general, the agreement with the results reported here is good.

The solid lines in Figs. 4–6 are the predictions of classical nucleation theory scaled to force agreement with the experimental data. The scaling was done in the following way: First, the ratio F was defined as

$$F = J_m/J_{\mathrm{BDZ}}, \tag{10}$$

where J_m is the measured nucleation rate and J_{BDZ} is the classical prediction for the corresponding supersaturation and temperature conditions. Then the scale factor F was assumed to be of the form

$$\ln(F) = -(w'/kT) = -(a - b/T). \tag{11}$$

In writing Eq. (11) we have arbitrarily suppressed the dependence of F on vapor supersaturation. Using Eq. (11), the expression for the nucleation rate can be written as

$$J_m = K(S, T)\exp[-(w + w')/kT]. \tag{12}$$

In Eq. (12), w is the reversible work of formation of a critical cluster, w' is the adjustment to w arising from the scaling factor in Eq. (11) and $K(S, T)$ is the usual prefactor employed in classical nucleation theory written

TABLE III. Values for the constants a and b used in Eq. (12) in the text for each of the alcohols. The appropriate temperature ranges are given in the text.

		a	b
ethanol	($T < 260$)	0	0
	($T > 260$)	121.28	31 434.8
n-propanol	($T < 275$)	−29.90	−9 976.9
	($T > 275$)	61.65	16 670.4
i-propanol		66.78	17 026.8

to indicate the dependence on supersaturation and temperature.

Values for the constants, a and b, appearing in Eq. (11) are listed in Table III for each of the alcohols. Using these constants and Eq. (12), the measured rate data shown in Figs. 4–6 can be reproduced to within a factor of 10 in all cases and usually to within a factor of 2.

The values of a and b can be used to predict the variation of critical supersaturation with temperature for the three alcohols which can then be compared with literature data. In Figs. 7–10 the variation of critical supersaturation with temperature for ethanol, n-propanol and i-propanol, respectively, is plotted. The solid circles in each figure represent data from this investigation. The experimental data corresponding to the solid circles is listed in Table IV. The open squares in Figs. 7 and 8 represent critical supersaturation data from the literature.[21] With the exception of the open squares in Fig. 8, the points in each plot were obtained in the following way: First, the supersaturation vs temperature profiles in the TDCC were obtained from experiments (or the literature) in which the rate of nucleation was roughly 1 drop/cm^3/s. Then, the BDZ nucleation rate expression was used to calculate the nucleation rate profile across the chamber. The values of S and T corresponding to the maximum calculated rate were then plotted in the figures. The open squares in Fig. 8 were taken directly from a plot in Ref. 24. Had Eq. (12) been used instead of the BDZ expression,

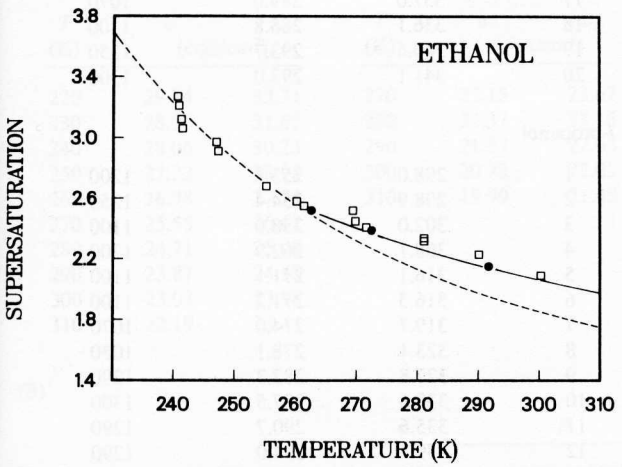

FIG. 7. Variation of the critical supersaturation of ethanol with temperature. The solid circles are the measured critical supersaturations, and the open squares represent literature data.[21] The dashed line is the BDZ prediction, and the solid line is obtained using Eq. (12) in the text and the appropriate values of a and b from Table III.

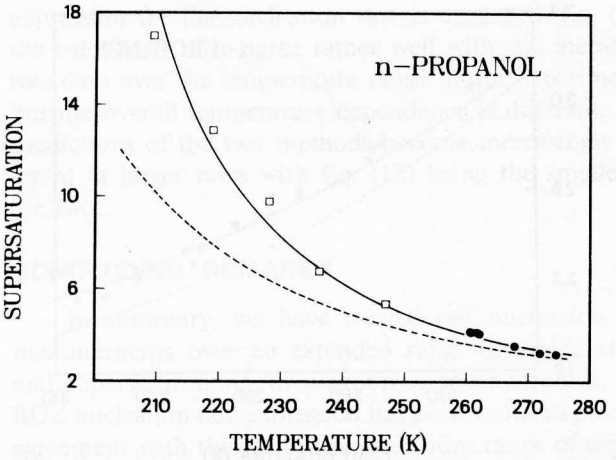

FIG. 8. Variation of the critical supersaturation of n-propanol with temperature below 275 K. The solid circles are the measured critical supersaturations from this investigation and the open squares are from the literature.[24] The dashed line is the BDZ prediction. The solid line is obtained using Eq. (12) and the appropriate values of a and b from Table III.

the resulting data points would not have differed greatly from those shown in spite of the fact the calculated maximum rate would have been closer to unity. This behavior is representative of the major disadvantage of critical supersaturation measurements and why it is important to have nucleation rate data.[26]

In Figs. 7–10 the dashed curves are the BDZ predictions, and the solid curves are obtained using Eq. (12) with J_m set equal to unity and the values of a and b from Table III. It should be remarked that, except for the n-propanol data shown for temperatures below 275 K in Fig. 8, the values of a and b used with Eq. (12) were obtained from the nucleation rate experiments. Figure 8 will be discussed below. The critical supersaturation data for ethanol appears to join the BDZ curve near 260 K; while the data for n-propanol in Fig. 9 appears to intersect the BDZ curve near 275 K. The i-propanol data is seen

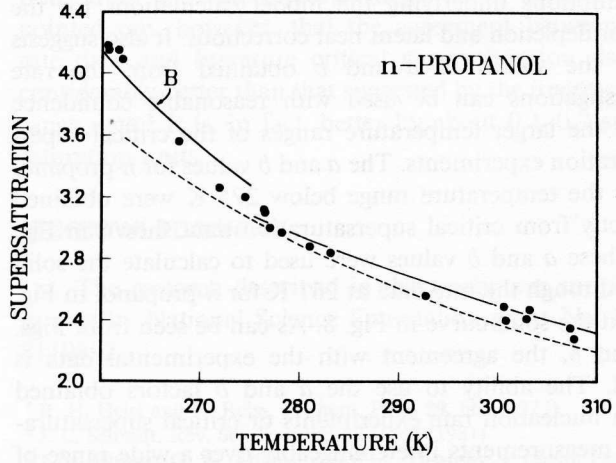

FIG. 9. Variation of the critical supersaturation of n-propanol with temperature above 275 K. The solid circles are the measured critical supersaturations and the dashed line is the BDZ prediction. The solid line is obtained using Eq. (12) in the text and the appropriate values of a and b from Table III. The solid line labeled B is a segment of the corresponding plot in Fig. 8.

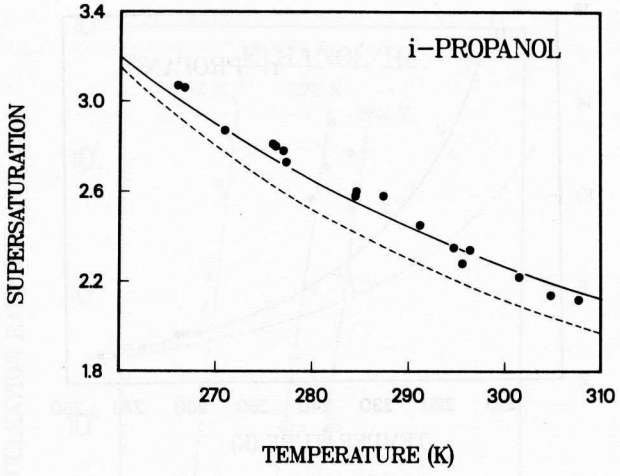

FIG. 10. Variation of the critical supersaturation of *i*-propanol with temperature. The solid circles are the measured critical supersaturations and the dashed line is the BDZ prediction. The solid line is obtained using Eq. (12) in the text and the appropriate values of a and b from Table III.

as tending toward the BDZ prediction at lower temperatures. If Eq. (11) is set equal to zero, corresponding to $F = 1$ in Eq. (10), the temperature at which the BDZ prediction and Eq. (12) agree is obtained for each alcohol. For ethanol this temperature is 259 K, for *n*-propanol the temperature is 270 K, and for *i*-propanol the temperature is 255 K, all in reasonable agreement with the critical supersaturation data.

It is possible to obtain values of a and b directly from critical supersaturation data. In essence, we would be using the rate data along the $\log(J) = 0$ line in the rate vs supersaturation plots. If we use literature values along with critical supersaturation data from this investigation, we obtain values of a and b which agree rather well with those obtained from the rate data. The two sets of constants generally agree to within 25% and in most cases to within 10%. This is reassuring since the critical supersaturation data were obtained in different laboratories, over larger temperature ranges and without the assumptions underlying the model calculations for the vapor depletion and latent heat corrections. It also suggests that the values of a and b obtained from the rate investigations can be used with reasonable confidence over the larger temperature ranges of the critical supersaturation experiments. The a and b values for *n*-propanol over the temperature range below 275 K were obtained directly from critical supersaturation data shown in Fig. 8. These a and b values were used to calculate the solid line through the rate data at 261 K for *n*-propanol in Fig. 5 and the solid curve in Fig. 8. As can be seen from Figs. 5 and 8, the agreement with the experimental data is good. The ability to use the a and b factors obtained from nucleation rate experiments or critical supersaturation measurements interchangeably over a wide range of temperatures and nucleation rates is also reassuring.

The critical supersaturation data for *n*-propanol appears to change slope in the 270–280 K range. This is particularly evident in Fig. 9 where, in addition to the experimental data obtained at temperatures above 275 K, a segment of the calculated critical supersaturation curve from Fig. 8 has been included (curve B) to illustrate the different slopes of the data obtained over the temperature ranges below and above about 275 K. The reason for this behavior is not clear at this point, although it may be related to vapor phase association. All of the lower molecular weight alcohols are known to undergo varying degrees of association in the vapor. We first noticed peculiar behavior during our nucleation rate experiments over this temperature range; and then, after carrying out the critical supersaturation experiments, confirmed this interesting behavior by discovering the change in slope. The critical supersaturation data for ethanol also appears to change slope but at a somewhat lower temperature near 260 K. The critical supersaturation data below

TABLE IV. Experimental measurables: T_L the temperature of the surface of the liquid pool; T_U the temperature of the top plate; and P_T the total pressure.

Run No.	T_L (K)	T_U (K)	P_T (mm Hg)
Ethanol			
1	291.3	250.2	1050
2	301.3	259.4	1090
3	320.6	278.4	1100
n-propanol			
1	295.0	248.2	1050
2	294.9	248.3	1050
3	296.3	249.2	1050
4	296.7	249.6	1000
5	302.0	255.7	1000
6	304.7	259.1	1000
7	307.8	261.6	1000
8	309.7	263.7	1050
9	309.8	263.6	1050
10	310.1	264.6	1000
11	311.2	265.7	960
12	313.1	267.5	1000
13	315.6	269.7	970
14	324.6	278.9	900
15	333.7	286.5	1000
16	333.3	286.8	1190
17	337.0	289.0	1070
18	336.1	288.8	1200
19	340.6	293.7	1250
20	341.1	293.0	1300
i-propanol			
1	298.0	253.8	1200
2	298.9	254.4	1250
3	302.0	258.0	1100
4	308.1	262.9	1200
5	316.1	271.1	1100
6	316.3	271.2	1100
7	319.7	274.0	1070
8	323.1	278.1	1050
9	327.8	282.3	1290
10	332.6	287.5	1300
11	335.6	290.7	1290
12	339.6	294.0	1290
13	309.3	264.1	1170
14	308.4	263.3	1170
15	309.3	264.5	1150
16	325.8	280.8	1200
17	326.1	281.9	1130

260 K appear to follow the BDZ prediction rather closely. In fact, using the values of a and b from Table III for the temperature range below 260 K, Eq. (12) can be used to predict the measured critical supersaturation data down to 206 K.[24]

It is of interest to note the change in the value of the bulk liquid surface tension necessary to bring the classical nucleation theory in agreement with the experimental data. In Table V(A) we list σ_a and σ for each alcohol at various temperatures. The value σ_a is the adjusted value of the bulk liquid surface tension necessary to bring nucleation theory and experiment into agreement. σ is the literature value of the bulk liquid surface tension obtained from the correlations in Table II. In all cases, over the temperature range investigated, it was necessary to increase the bulk liquid surface tension to obtain agreement between theory and experiment. If we define $\sigma^* = \sigma_a/\sigma$, we can correlate σ^* with temperature over the range of our experiments in the following way:

$$(\sigma^*)^3 = \beta \times T + \alpha, \tag{13}$$

where T is the temperature and α and β can be obtained from the critical supersaturation data. Values of α and β are given in Table V(B) for the three alcohols. If the BDZ expression for the nucleation rate is used with Eq. (13), the calculated rates agree rather well with the measured rate data over the temperature range of our experiments, but the overall temperature dependence is different. The predictions of the two methods become increasingly different at larger rates with Eq. (12) being the smaller of the two.

TABLE V. (A) The values of the surface tension σ_a necessary to bring the BDZ nucleation theory in agreement with experiment. The bulk liquid surface tension σ is obtained using expressions listed in Table II. (B) Values of α and β for each alcohol for use with Eq. (13) in the text.

(A)

Ethanol		
T (K)	σ (ergs/cm^2)	σ_a (ergs/cm^2)
260	25.04	25.20
270	24.16	25.03
280	23.28	24.79
290	22.40	24.52
300	21.52	24.20

n-propanol			*i*-propanol		
T (K)	σ (ergs/cm^2)	σ_a (ergs/cm^2)	T (K)	σ (ergs/cm^2)	σ_a (ergs/cm^2)
220	29.74	33.31	270	23.15	23.67
230	28.90	31.67	280	22.37	23.16
240	28.06	30.23	290	21.57	22.63
250	27.22	28.93	300	20.78	22.05
260	26.38	27.74	310	19.99	21.45
270	25.55	26.62			
280	24.71	25.00			
290	23.87	24.50			
300	23.03	23.98			
310	22.19	23.41			

(B)

		α	β
ethanol	($T > 260$)	−1.602	10.06×10^{-3}
	($T < 260$)	+1.000	0
n-propanol	($T > 275$)	−0.258	4.62×10^{-3}
	($T < 275$)	+2.559	-5.37×10^{-3}
i-propanol		−0.063	4.19×10^{-3}

CONCLUDING REMARKS

In summary, we have carried out nucleation rate measurements over an extended range of temperatures and supersaturations for a group of three alcohols. The BDZ nucleation rate expression has been scaled to produce agreement with this data over the entire range of experimental conditions. This scaled BDZ theory has been used to calculate the temperature dependence of the critical supersaturation, and the results are in good agreement with experimental data even at temperatures outside the range used for the nucleation rate investigation. We have observed changes in the slope of the temperature dependence of the critical supersaturation for ethanol and *n*-propanol at about 260 and 275 K, respectively. The scaling factors for the BDZ expression for each of these alcohols are different in the temperature ranges above and below these temperatures. The reason for this change in slope is not clear at this point.

We have compared our rate data and the predictions of Eq. (12) with results from two other investigations[3,27] and have found qualitative agreement in both cases. In the first, measurements were made at very high rates of nucleation of ethanol vapor and *n*-propanol vapor, e.g., 10^6–10^9 drops/cm^3/s, and in the second at intermediate rates of nucleation of ethanol vapor, e.g., 10^2–10^5 drops/cm^3/s. Predictions, based upon Eq. (12), agree reasonably well with most of the high rate data, although the data suggest that vapor depletion and latent heat effects may be important in the high rate data. The predictions based upon Eq. (12) have similar slopes but are shifted by about 0.1–0.2 supersaturation units toward higher supersaturations from the intermediate range data.[3] It should be pointed out, however, that the agreement between our rate data and literature critical supersaturation data is considerably better than that suggested by the intermediate range data.[3] It is, in fact, better by about 0.1–0.2 supersaturation units.

ACKNOWLEDGMENT

The research described in this paper was supported in part by National Science Foundation grant No. CPE-8119892.

[1] R. H. Heist and H. Reiss, J. Chem. Phys. **59,** 665 (1973).
[2] J. L. Schmitt, Rev. Sci. Instrum. **52,** 1749 (1981).
[3] J. L. Schmitt, G. W. Adams, and R. A. Zalabsky, J. Chem. Phys. **77,** 2089 (1982).
[4] J. L. Schmitt, R. A. Zalabsky, and G. W. Adams, J. Chem. Phys. **79,** 4496 (1983).
[5] R. Miller, R. Anderson, J. L. Kassner, Jr., and D. Hagen, J. Chem. Phys. **78,** 3204 (1983).
[6] P. E. Wagner and R. Strey, J. Phys. Chem. **85,** 2694 (1981).

[7] R. H. Heist, A. Fuchs, and G. Agarwal, Chem. Eng. Commun. **5,** 1 (1980).
[8] A. Fuchs, Master thesis, University of Rochester, 1979.
[9] J. Brito, Master thesis, University of Rochester, 1981.
[10] J. Brito and R. H. Heist, Chem. Eng. Commun. **15,** 133 (1982).
[11] R. H. Heist, A. Kacker, and J. Brito, Chem. Eng. Commun. **28,** 117 (1984).
[12] In the past the boiling point of the liquid under investigation was considered the upper limit of the accessible temperature range for the TDCC. With the development of a high pressure TDCC in the author's laboratory, this is no longer true. The critical point of a material is essentially the upper limit of accessibility for the TDCC. See, M. Heeks, Master thesis, University of Rochester, 1984, for details.
[13] J. L. Katz and B. J. Ostermier, J. Chem. Phys. **47,** 478 (1967).
[14] J. L. Katz, J. Chem. Phys. **52,** 4733 (1970).
[15] R. H. Heist and H. Reiss, J. Chem. Phys. **59,** 665 (1973).
[16] J. L. Katz, C. J. Scoppa, N. G. Kumar, and P. Mirabel, J. Chem. Phys. **62,** 448 (1975).
[17] J. L. Katz, P. Mirabel, C. J. Scoppa, and T. L. Virkler, J. Chem. Phys. **65,** 382 (1976).
[18] R. H. Heist, *Handbook for Heat and Mass Transfer Operations,* edited by N. Cheremisnoff (Gulf, 1985) Vol. 1, Chap. 19.
[19] See, e.g., S. K. Friedlander, *Smoke, Dust and Haze, Fundamentals in Aerosol Behavior* (Wiley, New York, 1977), Chap. 5.
[20] See, e.g., R. S. Bradley, M. G. Evans, and R. W. Whytlaw-Gray, Proc. R. Soc. London Ser. A **186,** 368 (1946); C. Rooth, Tellus **9,** 372 (1957); N. A. Fuchs, *Evaporation and Droplet Growth in Gaseous Media* (Pergamon, New York, 1959); N. Fukuta and L. A. Walter, J. Atmos. Sci. **27,** 1160 (1970).
[21] In Fig. 4 the open squares represent critical supersaturation data obtained from data in Ref. 13, and the open triangles represent critical supersaturation data from Ref. 22. The open triangle in Fig. 5 was obtained from Ref. 23. The open squares in Fig. 7 were obtained from data in Ref. 13, and the open squares in Fig. 8 were obtained from Fig. 1 in Ref. 24. The critical supersaturation vs temperature profiles in Ref. 13 were originally calculated with the Wassiljewa coefficients in the mixture thermal conductivity expression set to unity. We have recalculated the temperature and supersaturation profiles using the Lindsay–Bromley formalism for these coefficients. See Ref. 25 for additional details concerning the Wassiljewa coefficients. This is the reason the critical supersaturation data from Ref. 13 shown in our Figs. 4 and 7 appear different than in the original reference.
[22] C. S. DuPuis, Master thesis, University of Rochester, 1979.
[23] C. Flageollet, M. Dinh Cao, and P. Mirabel, J. Chem. Phys. **72,** 544 (1980).
[24] J. P. Garnier, P. Mirabel, and H. Rabeony, J. Chem. Phys. **79,** 2097 (1983).
[25] R. C. Reid, J. M. Prausnitz, and T. K. Sherwood, *The Properties of Gases and Liquids,* 3rd ed. (McGraw–Hill, New York, 1977), Chap. 10.
[26] The reason for using the BDZ rate expression to calculate the nucleation rate profile across the chamber instead of Eq. (12) is one of consistency. Our convention for determining the zone thickness and the no-nucleation concentration and temperature in the vapor depletion and latent heat model, e.g., Eqs. (1)–(4), is to use the BDZ expression.
[27] R. Strey (private communication).